

Jacquemart, M., et al., 2020, What drives large-scale glacier detachments? Insights from Flat Creek glacier, St. Elias Mountains, Alaska: *Geology*, v. 48, <https://doi.org/10.1130/G47211.1>

Supplementary Material

Mylène Jacquemart, Michael Loso, Matthias Leopold, Ethan Welty, Etienne Berthier, Jasmine S. S.

Hansen, John Sykes, Kristy Tiampo

S1. Satellite images and digital elevation models (DEM)	2
S2. DEM coregistration, detachment volume and error estimation	3
S2.1 DEM coregistration for DEM differencing	3
S2.2 Detachment & deposition volume estimation	4
S2.3 Error estimation	8
S3.3 Regional elevation trend since 2000	9
S3. Permafrost distribution	10
S4. Velocity estimation	13
S4.1 Velocity estimation from flow runup	13
S4.2 Velocity estimation from superelevation	14
S4.3 Velocity estimation from seismic data	14
S5. Bulge thickness and advance	16
Bulge thickness calculation	16
Bulge advance	18
S6. Water availability calculation	20
S6.1 Bias-correction	20
S6.2 Water availability calculation	21
S7. Flow accumulation analysis	22
S8. Grain size distributions	22
S9. Seismic data	23
S10. Tree core data	23
S11. Data analysis and processing code	24
S12. Supplementary materials references	24

S1. Satellite images and digital elevation models (DEMs)

Because the 2013 and 2015 detachments at Flat Creek were not witnessed by anyone, we largely reconstructed the events from remotely sensed data. Table 1 lists all satellite images and DEMs that were used in this study. Pre- and post-detachment glacier margins were manually mapped on cloud free images. We traced the areas of the glacier affected by the detachments and the outlines of the subsequently formed deposits from DEM difference maps (dH maps) and in optical images. Optical images were used where the contrast between the impacted area and vegetated areas was clearly visible. Where the contrast was not sufficient, we used the signals in the dH maps.

We used DEMs from ArcticDEM (Porter et al., 2018) and an Alaska-wide Interferometric Synthetic Aperture Radar (IFSAR) survey . The IFSAR data consists of a 5 m DEM, the data for which was acquired between 2012-08-14 and 2012-09-08. In the main article, we denote the date of this DEM as 2012-08-26 rather than $2012-08-26 \pm 12$ days. Both a digital surface model (DSM), generated from X-band (3 cm center wavelength) data, and a digital terrain model (DTM), generated from P-band data (80 cm center wavelength) data, are available. The ArcticDEM strips are DSMs generated from stereo optical images (Worldview satellite imagery) available from the Polar Geospatial Center (PGC). In order to minimize effects from the different acquisition techniques (optical vs. radar) and radar penetration into the snowpack, we used the X-band generated IFSAR DSM for all DEM differencing. Its acquisition in mid-August to early September, when meltwater is abundant in the snow and firn, should minimize radar penetration.

Data type	Acquisition date	Resolution	Description	Source
Optical image	2009-07-13	0.8 m	Ikonos raw image, orthorectified with Alaska IfSAR DEM.	©Maxar
Optical image	2010 - 2016	5 m	Rapid Eye Orthophotos, 38 images	Planet Labs, https://www.planet.com/explorer/

DSM	Data acquired between 2001-06-08 and 2018-09-25	30 m	ASTER DEMs, 128 scenes	Generated from L1A raw ASTER images https://earthdata.nasa.gov
DSM	Data acquired between 2012-08-14 and 2012-09-08	5 m	Alaska wide IfSAR DEM	USGS / The National Map Server https://www.usgs.gov/core-science-systems/ngp/tnm-delivery/
DSM	2014-10-12	2 m	ArcticDEM strip	Polar Geospatial Center https://www.pgc.umn.edu/data/arcticdem/
DSM	2015-09-08	2 m	ArcticDEM strip	Polar Geospatial Center https://www.pgc.umn.edu/data/arcticdem/
DSM	2016-03-13	2 m	ArcticDEM strip	Polar Geospatial Center https://www.pgc.umn.edu/data/arcticdem/

Tab. 1: Summary of datasets used in this study.

S2. DEM coregistration, detachment volume and error estimation

S2.1 DEM coregistration for DEM differencing

We followed the methods described by Nuth & Kääb (2011) to coregister the DEMs to each other and used Matlab code by Ian Howat to perform this coregistration

(https://github.com/ihowat/setsm_postprocessing/blob/master/coregisterdems.m). This simple method identifies systematic shifts between DEMs by plotting DEM differences against terrain slope and aspect (Nuth & Kääb, 2011). The shift between these parameters is minimized iteratively, until the improvement in root mean square error (rmse) between one iteration and the next is smaller than 0.001 m. We coregistered all other DEMs to the reference 2014 ArcticDEM. All glaciated areas and areas affected by the failures were masked in the reference DEM to prevent coregistration over actively changing surfaces. We created the glacier mask by adding a 225 m buffer to the Randolph Glacier Inventory (RGI) 6.0 outlines (RGI Consortium, 2017). The final RMSE for the 2012, 2015, and 2016 DEMs was 1.05 m, 0.78

m, 0.81 m, respectively. DEM difference (dH) maps were then produced by subtracting the pre-detachment DEM from the post-detachment DEM.

S2.2 Detachment & deposition volume estimation

Detachment volumes

To quantify the detachment volumes, we manually delineated the areas affected by the detachments in the dH maps and used those outlines to integrate the total volumetric loss (dV). We provide an upper and lower bound dV estimate for the following reason: Satellite images after the 2013 detachments show that the remaining glacier advanced by 30-45 m between 2013-08-11 and 2013-09-05, in response to the frontal debutressing caused by the detachment. This advance is followed by disintegration of the remaining ice cliff and accumulation of ice debris below the new terminus, a process that can be observed throughout 2014 and into early 2015. Due to this accumulation of loose ice, the 2014-10-12 DEM does not show the full depth of erosion caused by the detachment, but a surface that has been partially re-covered by ice (see Fig. S1 and S2). Coinciding with the observed advance and disintegration of the glacier front, we see widespread thinning on the remaining glacier that is not visible on neighboring glaciers. We consider the amount of thinning observed upstream of the detachment line as a proxy for the maximum ice volume deposited in the detachment zone between 2013-08-05 (the day of the 2013 detachment) and 2014-10-12 (date of the DEM acquisition). Based on the known occurrence of this post-detachment mass transfer, we calculate both a lower bound and upper bound volumetric loss for the ice detachment. The lower bound only considers the elevation difference in the detachment zone. The upper bound further includes the thinning of the upper glacier as an estimate of the volume that advanced into the detachment zone in response to the collapse.

In addition to the ArcticDEM from 2016-03-13, a DEM from 2015-09-08 is available from the PGC. This DEM lacks coverage of the upper part of the ridge included in the failure, but it was acquired

only 40 days after the 2015-07-31 detachment. It offers an estimate of detachment volumes where response by the glacier and surrounding landscape to the surface change are minimized. Differencing this DEM from the 2014-10-12 DEM yields a detachment volume between $18.0 \pm 0.2 \times 10^6 \text{ m}^3$ and $19.9 \pm 0.4 \times 10^6 \text{ m}^3$. This minimum estimate is slightly higher than the one presented in the main article ($17.6 \pm 0.2 \times 10^6 \text{ m}^3$), which was obtained from differencing the 2014-10-12 DEM with the one from 2016-03-13. Given that the 2015-09-08 DEM does not cover the total area of the detachment (see Fig. 3), the difference between the two lower bound detachment volumes indicates that the number presented in the main article is a conservative estimate.

Deposition volumes

To estimate the deposition volumes, we used the same techniques as described for the detachment volumes. However, due to the presence of both depositional and erosional features in the runout zone, we classified all cells of the dH map within the runout outline as either erosion ($dH < 0$) or deposition ($dH > 0$). We then separately summed the height differences in the erosion cells and the deposition cells. The results are listed in Tab. 2.

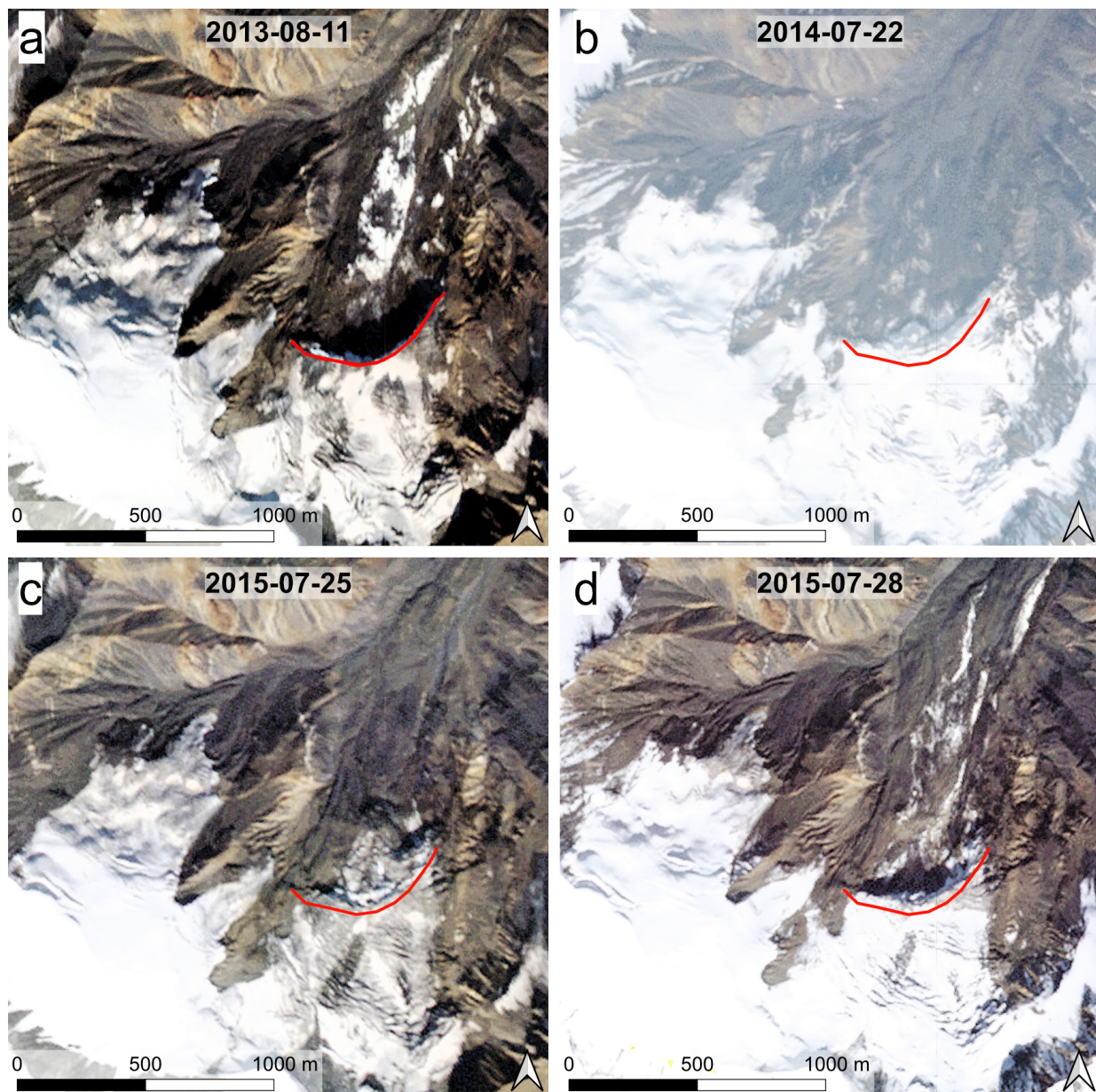


Fig. S1: a) Image six days after the first detachment in 2013 (2013-08-11). The detachment line is marked red and repeated in all four images. b) Image from 2014-07-22. Note the advance of the terminus past the detachment line. c) Image from 2015-07-25. Note the continued advance and accumulation of loose ice in the detachment zone. d) Image from 2015-07-28. The accumulated ice has detached. All images © Planet Labs (Planet Team, 2018).

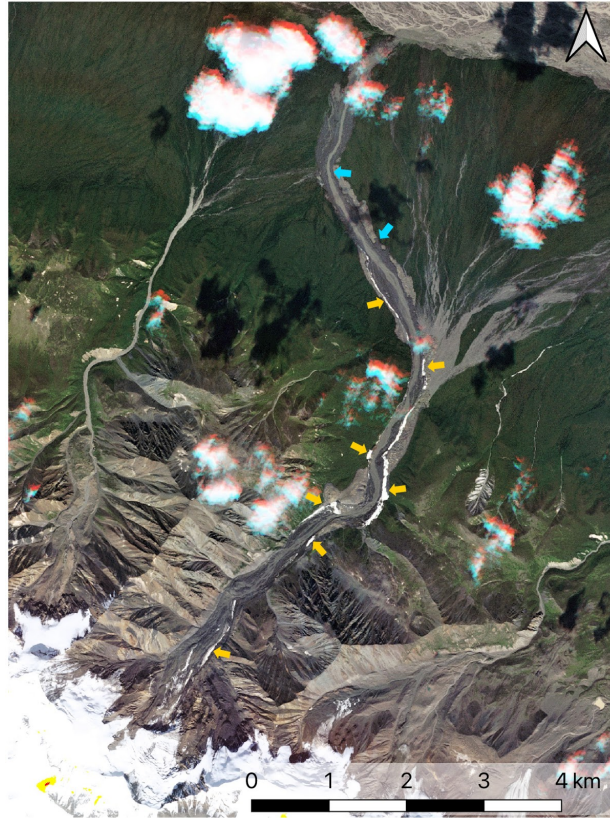


Fig S2: Shortly before the 2015 detachment, ice that had accumulated downstream of the 2013 detachment line detached and travelled ~10 km downstream. Yellow arrows indicate fresh ice deposits, blue arrows indicate fresh debris deposits. Planet Labs image from 2015-07-25.

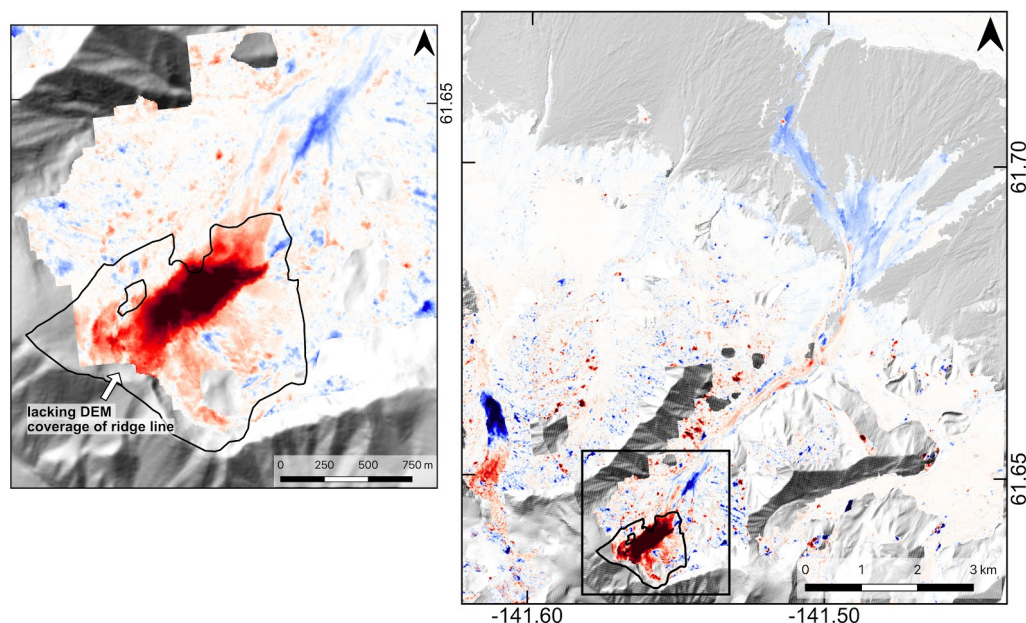


Fig. S3: dH map produced by differencing the Arctic DEMs from 2015-09-8 and 2014-10-12.

	Total erosion	Total deposition	Net deposit
2013	$1.9 \pm 0.65 \times 10^6 \text{ m}^3$	$9.1 \pm 1.1 \times 10^6 \text{ m}^3$	$7.2 \pm 1.7 \times 10^6 \text{ m}^3$
2015	$2.8 \pm 0.39 \times 10^6 \text{ m}^3$	$17.5 \pm 1.0 \times 10^6 \text{ m}^3$	$14.7 \pm 1.2 \times 10^6 \text{ m}^3$

Tab. 2: Total erosion, deposition and net deposit volumes for the 2013 and 2015 Flat Creek glacier detachments.

S2.3 Error estimation

To estimate the error bounds of our volume estimates, we applied the approach described in Miles et al. (2018) and Berthier et al. (2016). First, we masked the dH maps to retain only stable terrain, then divided these stable areas into $n \times n$ tiles, where n is set to increase from 2 to 200. For each tile, the median absolute dH is calculated, then an average dH is computed for each tile size. The relationship between mean error and tile size is well-represented by a logarithmic fit, which we used as our error model to estimate the expected mean error of dH for a given area (i.e., of a detachment). Multiplying the error for dH by the area yields the expected volumetric (error see example in Fig. S4).

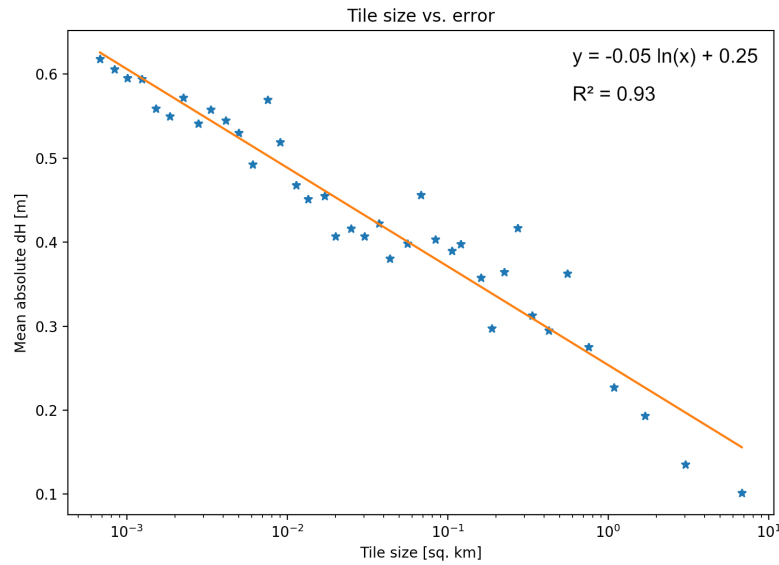


Fig. S4: Error function derived from tiled stable area for 2016 minus 2014.

S2.4 Regional elevation trend since 2000

We generated 128 DEMs from L1A ASTER images using the open-source Ames Stereo Pipeline routine (Shean et al., 2016). To study the regional mass balance of glaciers in the Flat Creek area, we used the ASTERIX processing chain (e.g. Dussaillant et al., 2019). As elsewhere in Alaska, regional elevation changes (Fig. S5) are predominantly negative (mass balance for this 3760 km² glacierized area is -0.32 ± 0.04 m yr⁻¹ water equivalent). Against the general trend of decreasing surface elevation, surging glaciers locally cause large elevation increases. The range of dH/dt (rate of change of surface elevation) is -30 m/yr up to 57 m/yr. This is evidenced by several large surging glaciers in the area, as well as by the glacier in the drainage west of Flat Creek (see Fig. 3 in main article and Fig. S3) which shares a drainage divide with Flat Creek Glacier and commenced a surge around 2012, advancing approximately 1 km.

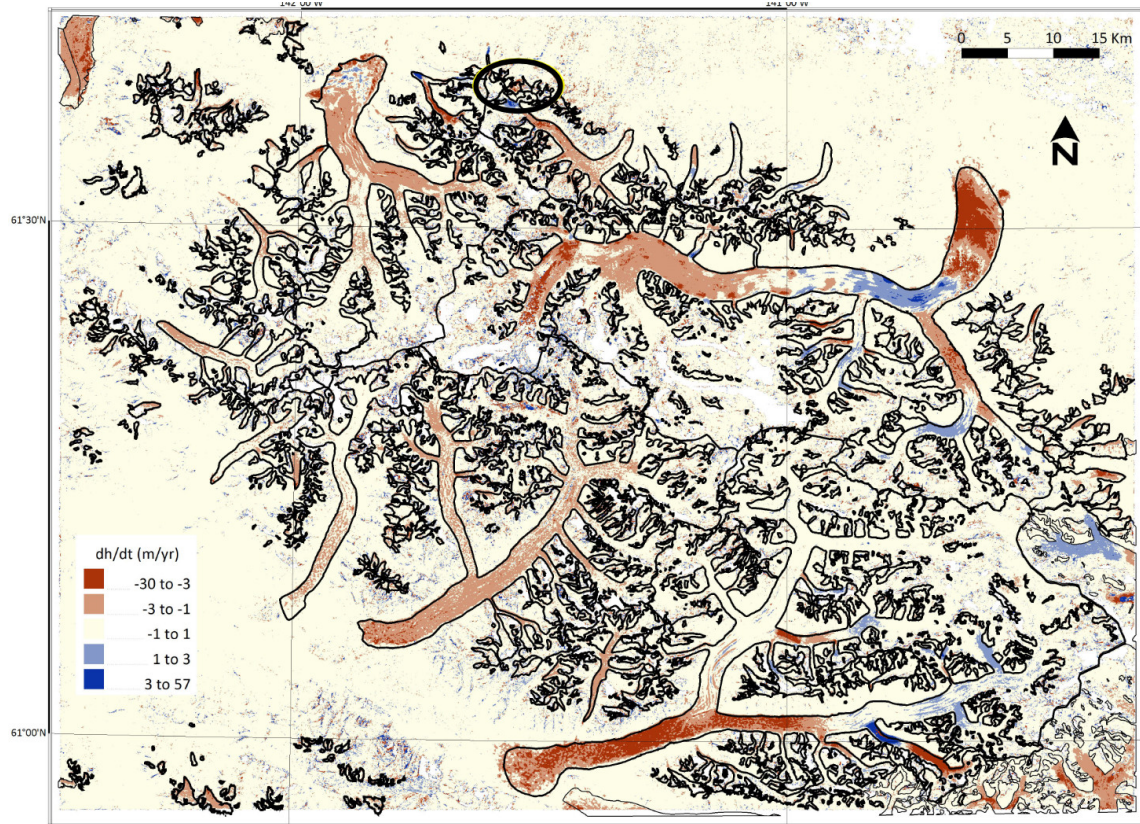


Fig. S5: Regional rate of glacier elevation changes between 2002 and 2018 computed from 128 ASTER DSMs. Glacier outlines (black) are from the Randolph Glacier Inventory 6.0, the Flat Creek Glacier area is circled.

S3. Permafrost distribution

We investigated the occurrence of ice rich permafrost along three transects in Flat Creek Valley between 2019-07-28 and 2019-08-04 using electrical resistivity tomography (ERT). We used a multi-electrode system from Lippman Geophysical Instruments (4punktlight hp; Lipmann 2008) with up to 40 electrodes and a combined Wenner and Dipole-Dipole array. Each point was measured three times with a maximum difference of 2% between measurements. Points exceeding 2% difference were measured a total of five times and subsequently averaged. Points differing more than 5% were deleted. The measurement frequency was 5Hz and applied currents were 0.1 mA to 5.0 mA, which resulted in measured voltages of

1–108 mV. We used RES2DINV software (Loke 2013) to invert the apparent resistivity values and produce a 2-D model of the specific electric resistivity of the subsurface. Results from the three surveys are shown in Figure S6.

Additionally, hourly ground temperatures were measured at 0 m, 0.25 m, ~0.5 m and ~0.75m below the ground surface for 335 days from 2018-07-06 to 2019-06-06 (when the logger was destroyed, presumably by wildlife). The measured mean temperatures (which may differ slightly from mean annual temperatures due to the subannual measurement period) were -3.19 °C, -3.57 °C, -2.95 °C, and -3.05 °C, respectively. When the logger was installed in July 2018, the temperature in the deepest borehole was 1.16 °C, while the temperature at the ground surface was 17.12 °C (Fig. S7).

These data show good agreement between the results of the ERT survey (Fig S6c) and the ground temperature data (Fig. S7), which were measured in the same location: The ERT survey indicates an active layer depth of about two meters, and we measured temperatures around 1 °C during installation at less than 1 m depth. At the lower elevation site (1650 m asl, Fig. S6b), active layer depth is on the order of 5-10 m on the NE facing slope. We were unable to detect the permafrost table on a site with flat ground with slightly lower elevation (1580 m asl, Fig. S6a). While the measured temperatures and active layer depths are somewhat dependent on the measurement dates, these measurements indicate that permafrost is abundant and widespread at higher elevations and on shaded aspects.

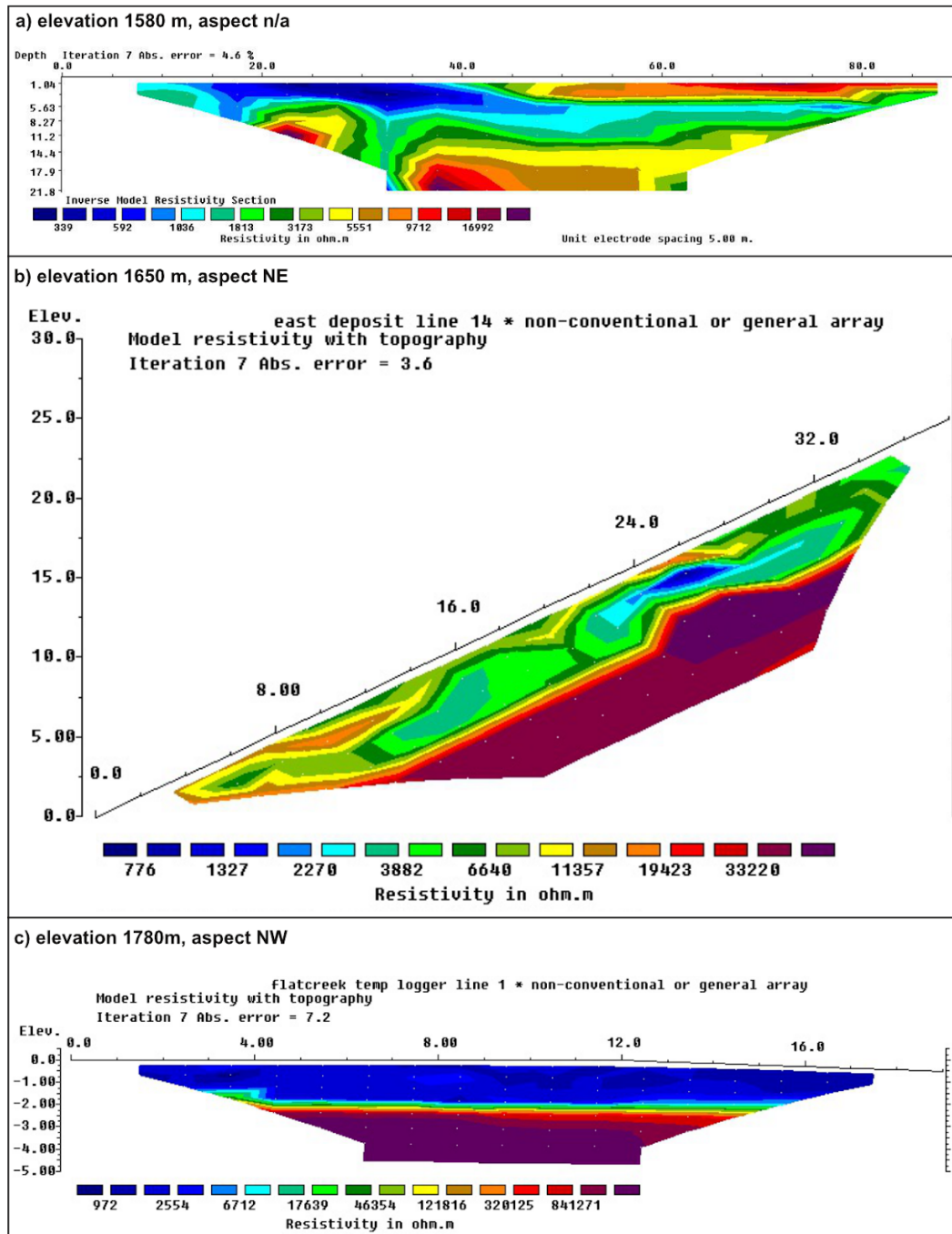


Fig. S6: Results from three ERT cross-sections in the Flat Creek watershed at different elevations. Red colors indicate high resistance to the flow of electric current, blue colors denote lower resistance (higher conductivity). Profiles b) and c) display clear, rapid transitions from a highly conductive to a highly

resistive subsurface, a pattern that we associate with a transition from the active layer into ice rich permafrost.

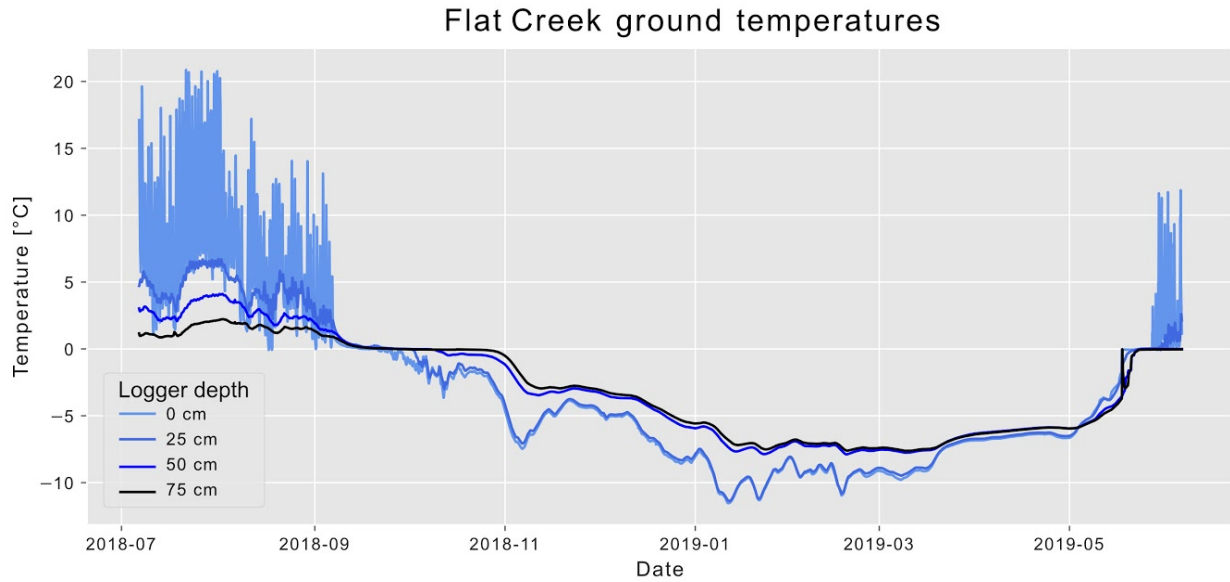


Fig. S7: Temperature measurements from ground temperature loggers placed at depths of 0 m, 0.25 m, 0.5 m and 0.75 m, measured at the same location of the ERT profile shown in Fig. S6c.

S4. Velocity estimation

We estimated local peak flow velocities at West Hill from flow runup and superelevation data, and mean flow velocities from seismic data. While these measurements represent different velocities at different locations, they all support the claim that the detachments rapidly transformed into highly mobile mass flows. The results are summarized in Fig. S8.

S4.1 Velocity estimation from flow runup

Both the 2013 and 2015 flows overtopped West Hill (see main article). By applying a simple frictionless point mass model (Iverson et al., 2016), we estimated the local flow velocities on the upstream side of West Hill as

$$u = \sqrt{2hg}, \quad (1)$$

where u is the flow velocity, h is the runup height on West Hill, and g is the gravitational acceleration. We estimated h by extracting ten elevation profiles from upstream of West Hill and over its highest point. The same ten profile lines were used for the 2013 and 2015 events, but we extracted the elevation data from the 2012 and 2014-10-12 DEMs, respectively.

S4.2 Velocity estimation from superelevation

In 2015, the flow banked steeply when it flowed around West Hill. We applied the most common formulation of the forced vortex equation (e.g., Scheidl et al., 2014, Prochaska et al., 2008),

$$u = \sqrt{\frac{Rg}{B} \Delta h}, \quad (2)$$

where u is the flow velocity, R is the channel's radius of curvature, g is the gravitational acceleration, B is the channel width, and Δh is the superelevation height. We estimated the mean superelevation height by digitizing the trim lines around West Hill and averaging the superelevation heights of five 200 m bins. This yielded superelevation heights ranging from 27.3 m to 79.8 m. River channel widths varied from 538 m to 886 m, and we determined eight different curvature radii varying from 951 m to 2260 m.

S4.3 Velocity estimation from seismic data

Between 2013 and 2016, six individual ground shaking events associated with large mass movements were recorded at the Barnard Glacier seismic station (see Fig. S9), approximately 60 km SSW of Flat Creek Glacier. All the waveforms have the characteristics of landslides, and they lack the clear P- and S-wave arrival times typical for earthquakes (Ekström & Stark, 2013). The seismic data was not used to locate the source of the shaking events, but the timing offsets of the waveforms at the different seismic stations line up correctly for the source to be located at Flat Creek (personal communication, Kate Allstadt, U.S. Geological Survey). Combined with the evidence from satellite imagery (and accounts by

local residents; Jacquemart & Loso, 2019), we are extremely confident that the recorded shaking events stem from the Flat Creek Glacier detachments. We estimated the duration of the ground shakings from the seismic data and then used the measured travel distances to calculate their mean velocities. We performed this analysis for the detachments on 2013-08-05 and the main detachment on 2015-07-31 at 17:25 local AK time (Fig. S9).

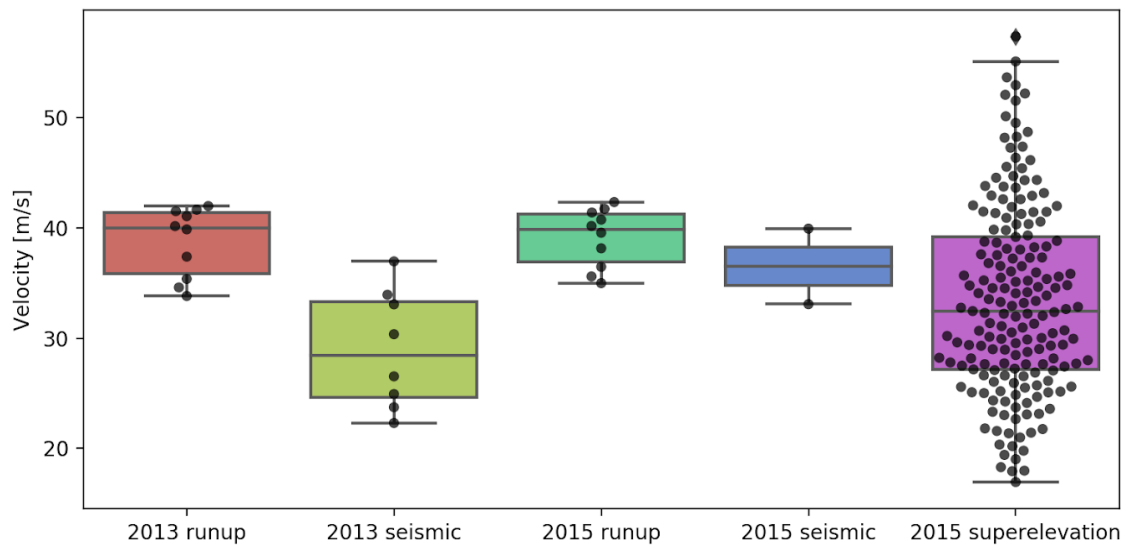


Fig. S8: Velocities of 2013-08-05 and 2013-07-31 glacier detachments estimated from runup, seismic and superelevation data.

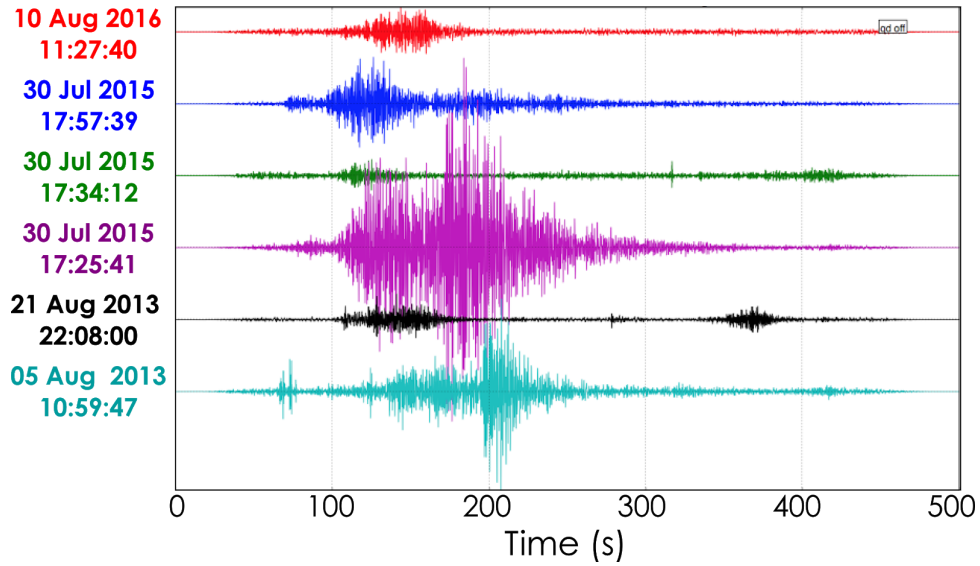


Fig. S9: Seismic record of all events at Flat Creek in local Alaska time, recorded at Barnard Glacier seismic station. Data courtesy of Kate Allstadt, USGS. Note that we omit the 21 August, 2013 and the 10 August, 2016 events from analysis due to their small sizes. Furthermore, we treat the three events on 30 July 2015 as one event.

S5. Bulge thickness and advance

S5.1 Bulge thickness calculation

We estimated the thickness of the bulge on Flat Creek Glacier based on the shadow that it cast on the glacier tongue below. A schematic of the relevant variables is shown in Fig. S10.

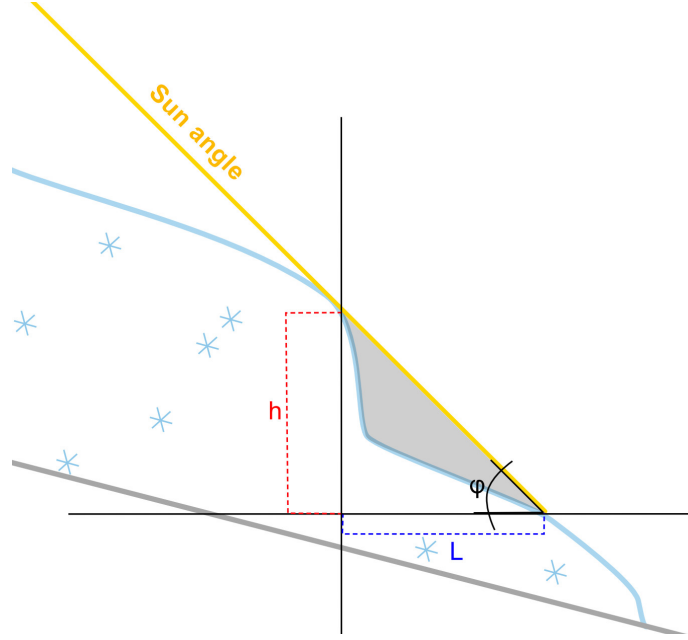


Fig. S10: Schematic of how shadow lengths were used to calculate the height of the bulge. All terms are explained in the text.

We calculated the incidence angle ϕ and azimuth of the sun's rays from the time and date of the image acquisition, as specified in the image metadata, and measured the length of the shadow L in the direction of the sun's azimuth (see Fig. S10). Consequently,

$$h = L * \arctan(\phi) \quad (3)$$

where h is the height of the bulge above the lower edge of the shadow. For each measurement, we assumed an uncertainty of \pm two pixels in the digitization of the shadow lengths (1.6 m for Ikonos). This leads to uncertainties of ± 9.4 m.



Fig. S11: Measured shadow lengths (red lines) on 2009 Ikonos image.

S5.2 Bulge advance

Comparing the image from 2009 to images from 2012 and 2013 (Fig. S12) show the emergence of a new feature casting a shadow on the tongue of Flat Creek Glacier. This feature first became apparent in summer 2012 and remained persistent through 2013, regardless of snow conditions. Under similar lighting conditions, the shadow cast by the bulge in 2009 was no longer continuous. This indicates that the distinct bulge visible in 2009 was no longer present in 2013. The detachment occurred 44 days after the acquisition of the image in Fig. S12d.

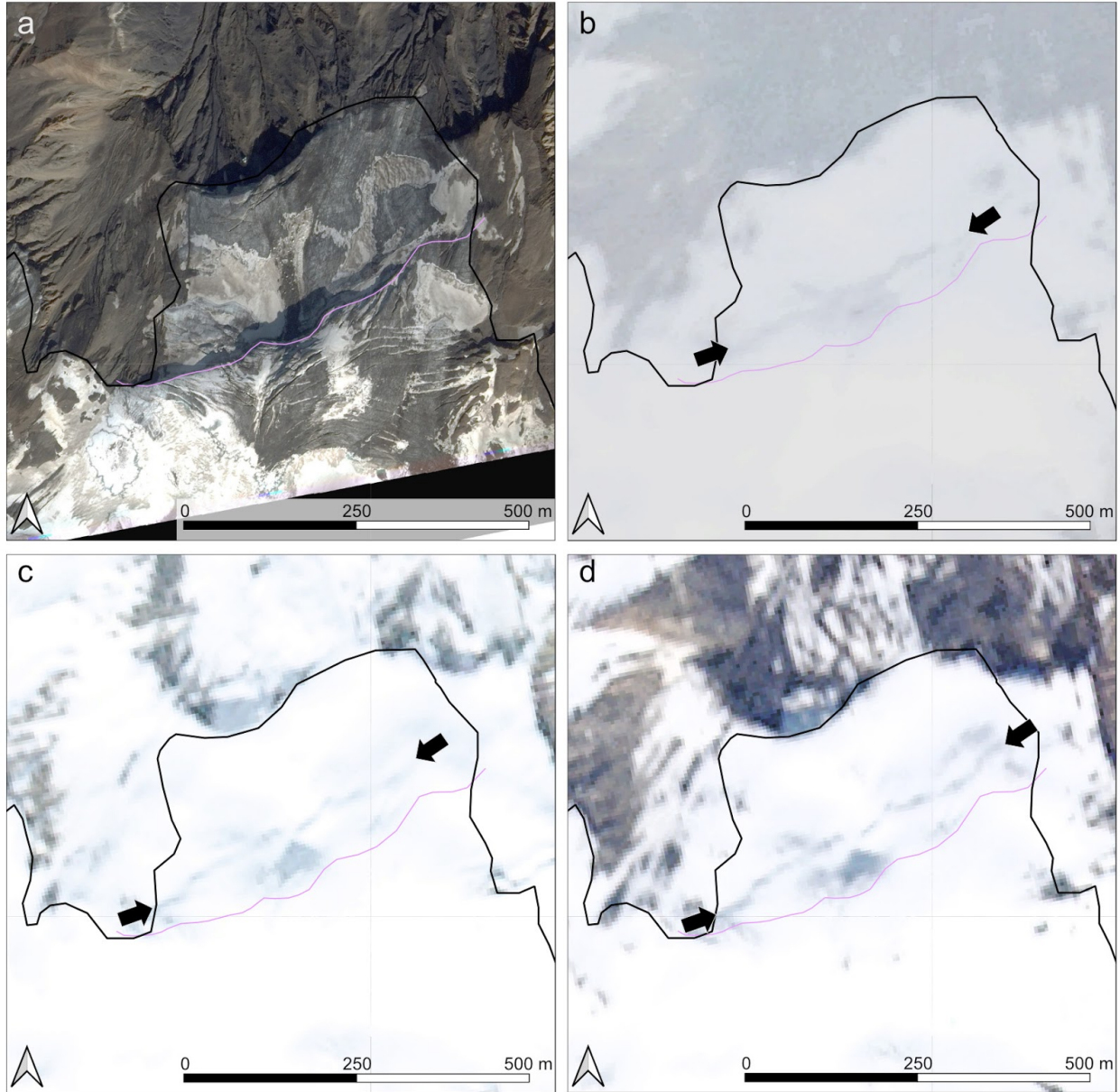


Fig. S12: Advance of the bulge. a) Ikonos image from 2009-07-13, b) Planet image from 2012-07-14, c) Planet image from 2013-05-23, d) Planet image from 2013-06-22. The pink line indicates the upper edge of the bulge in 2009 (image a).

S6. Water availability calculation

S6.1 Bias-correction

The weather station in Chisana (50 km NW of Flat Creek Glacier) is part of the Snow Telemetry (SNOTEL) Network maintained by the US Department of Agriculture's National Water and Climate Center. We downloaded all daily temperature and precipitation data back to 2008-07-06 from <https://wcc.sc.egov.usda.gov/nwcc/site?sitenum=1093>. To process a longer time-series, we downloaded temperature (2 m above ground) and precipitation data dating back to 1979 from <https://registry.opendata.aws/wrf-alaska-snap/>. These climate data have been dynamically downscaled for the state of Alaska from the European Centre for Medium-Range Weather Forecasts' interim reanalysis (ERA-Interim) dataset and are available at a spatial resolution of 20 km and hourly temporal resolution (Bieniek et al., 2016). As recommended by Bieniek et al. (2016), we use the ten years of data available from the Chisana SNOTEL station to identify and correct for any biases in the downscaled data.

The Chisana SNOTEL station is located at 1011.9 m above sea level (asl), and the mean elevation of the downscaled ERA grid cell at Chisana is 1586.5 m asl. Therefore, we first apply a lapse rate correction of 6 °C / km to the downscaled data to bring it to the same elevation as the SNOTEL station. We use a least-squares optimization to find the best fit between the station and the reanalysis data. The R-squared value for the fit of a quadratic regression between mean daily station temperature and mean daily reanalysis temperature is 0.92, which is a slight improvement over a linear regression with an R-squared of 0.90. We do not apply any corrections to the precipitation data because there is no evident, systematic offset between the two datasets.

S6.2 Water availability calculation

We applied the bias correction derived for Chisana to the downscaled reanalysis data over Flat Creek and calculate the water availability at 100 m elevation intervals between 2000 m asl and 2700 m asl. To derive the water availability, we assume that for any time-step i ,

$$H_i = M_i + P_{liq} , \quad (4)$$

where H is the total water availability, M is the total liquid water contribution from snow and ice melt, and P_{liq} is total liquid precipitation (all in mm). All precipitation that falls at temperatures above 0 °C is considered liquid precipitation. We calculate the contribution from snow and ice melt by applying a degree-day approach (Hock, 2003). This simple method relates the amount of snow and ice melt (M) to the sum of positive temperatures (T^+) during each time interval (Δt). The degree-day factor (DDF) is expressed in $\text{mm d}^{-1} \text{ } ^\circ\text{C}^{-1}$ and applied as follows:

$$\sum_{i=1}^n M = DDF \sum_{i=1}^n T^+ \Delta t . \quad (5)$$

Degree-day factors are commonly defined empirically and vary strongly from site to site. We do not have any local measurements from Flat Creek Glacier; instead, we use factors determined by the National Park Service Inventory and Monitoring Program on Kennicott Glacier (Fig. 1, main article). The derived DDFs of $2.70 \text{ mm d}^{-1} \text{ } ^\circ\text{C}^{-1}$ for snow and $4.87 \text{ mm d}^{-1} \text{ } ^\circ\text{C}^{-1}$ for ice agree closely with values determined at other glaciers in similar climatic zones around the world (i.e., Hellstugubreen, Norway). The DDF for snow was applied for as long as there was snow available for melt in any given water year. When the cumulative melt surpassed the snow accumulation, the DDF for pure ice was applied. To take into account diurnal variability in local temperature, we ran our model at hourly resolution from 1979 to 2016.

S7. Flow accumulation analysis

To analyze flow accumulation in the catchments of the three small glaciers located in the Flat Creek watershed, we used a Rho8 approach (Fairfield & Leymarie, 1991) implemented as part of the python package *richdem* (Barnes, 2016). Fig S13 shows the results of the flow accumulation analysis. Most notably, the area with the highest flow accumulation lies immediately above the detachment line. The second and third highest flow concentrations lie in the trough on the western side of the detachment, under the cold-ice tongue.

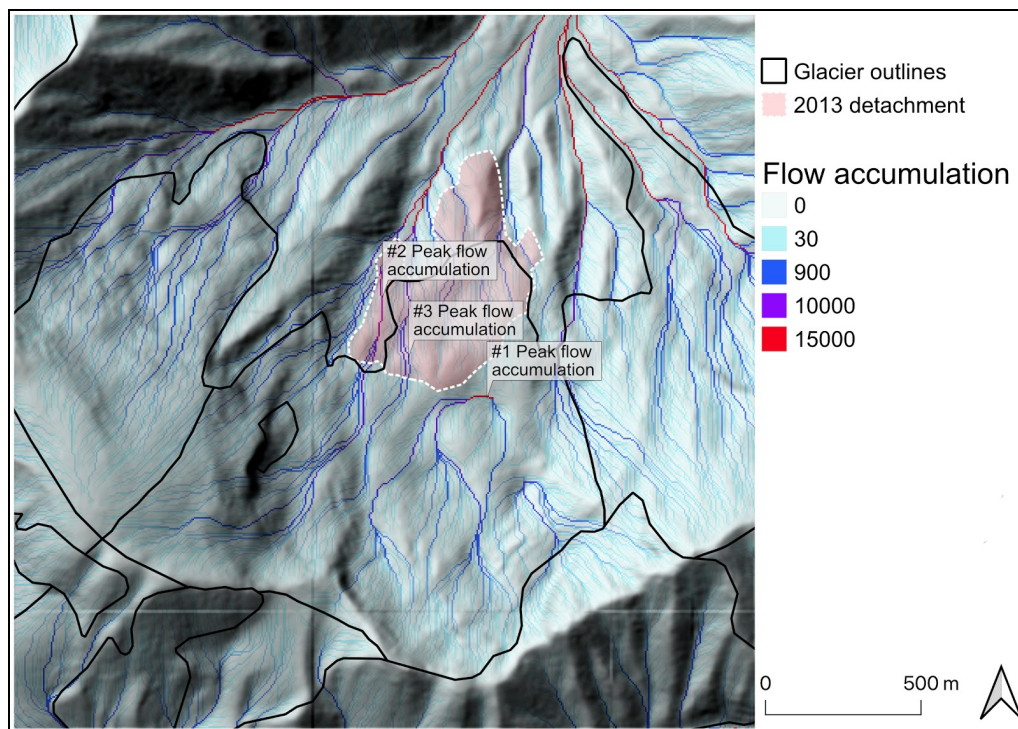


Fig. S13: Results of the flow routing analysis. Areas with the three highest flow accumulations are labeled accordingly. Data plotted on hillshade from 2012 (Alaska IfSAR DEM).

S8. Grain size distributions

We performed a wet sieving analysis on six sediment samples collected from various locations in Flat Creek valley during the 2018 field campaign (see Fig. 1, main article). All samples were dried in an oven

for 24 h after sieving. Five samples originated from the detachment deposit while one sediment sample (sample 6) originated from the original floodplain in the Flat Creek alluvial fan. For this analysis, we only considered the fine fraction of the samples because the limited time and sampling volume in the field did not allow us to adequately sample the larger grain sizes (Fig. S14).

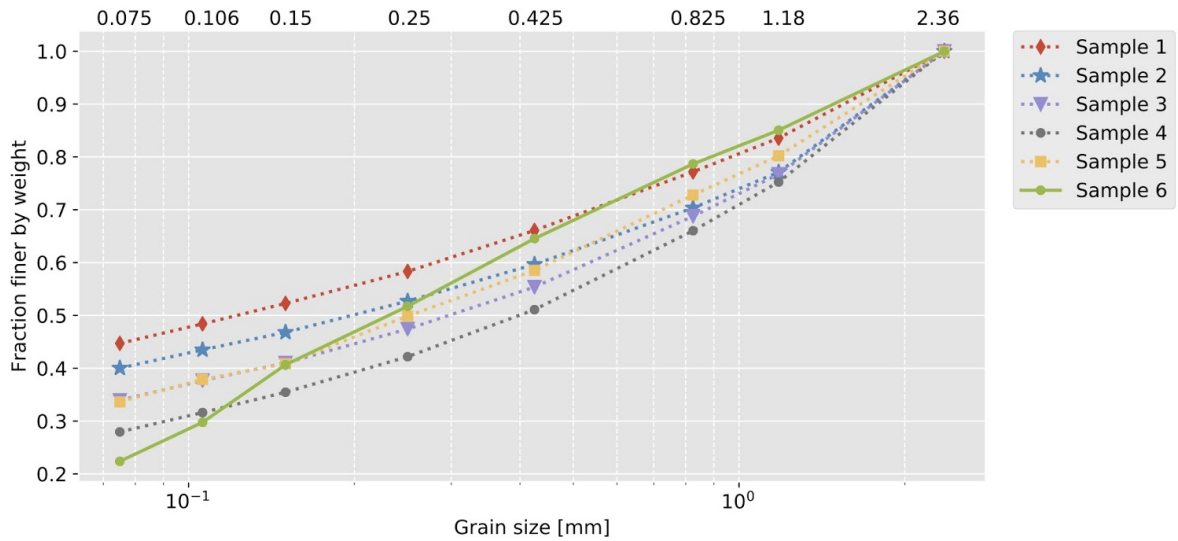


Fig. S14: Results from wet sieving analysis of five sediment samples collected from the debris deposits (see Fig. 1 for locations) and one from the previously existing floodplain (sample 6).

S9. Seismic data

To assess whether an earthquake could have caused the Flat Creek Glacier detachments, we applied the criterion described in Kääb et al. (2018): The U.S. Geological Service earthquake catalog does not list any earthquakes with magnitudes greater than 4 within 10 km, magnitudes greater than 6 within 100 km, or magnitudes greater than 8 within 1000 km.

S10. Tree core data

We determined the minimum age of the forest on the Flat Creek alluvial fan by coring 14 trees. Results are listed in Table S1.

#	Total Age	Confidence Interval	Counted rings	Estimated rings to pith	Measured length (mm)	Species	Field DBH (mm)	Coring height (mm)	Lat	Long
1	208+	unknown	208	unknown	75	Pigl	360	0	61.685079	-141.472642
2	169+	unknown	169	unknown	128	Pigl	265	0	61.685079	-141.472642
3	162	8	157	5	128	Pigl	230	0	61.685079	-141.472642
4	63	3	61	2	60	Pigl	690	0	61.685079	-141.472642
5	20+	unknown	20	unknown	50	Pigl	710	0	61.685079	-141.472642
6	31	2	30	1	70	Pigl	830	0	61.685079	-141.472642
7	148	7	148	0	75	Pigl	132	0	61.685079	-141.472642
8	165	8	165	0	130	Pigl	260	0	61.685079	-141.472642
9	125	6	125	0	62	Pigl	unknown	0	61.685079	-141.472642
10	325	16	323	2	90	Pigl	214	450	61.67317	-141.493435
11	268	13	268	0	100	Pigl	207	550	61.67317	-141.493435
12	275	14	275	0	117	Pigl	228	460	61.67317	-141.493435
13	396	20	396	3	190	Pigl	292	650	61.67317	-141.493435
14	259	13	259	0	100	Pigl	220	570	61.67317	-141.493435

Table S1: Dated ages of sampled tree cores. Red numbers denote minimum ages.

S11. Data analysis and processing code

All python code used to generate the results and figures presented in this manuscript are open-source and available at <https://github.com/mjacqu/FlatCreekProject>. This GitHub repository will be archived with Zenodo and a DOI will be added here before publication.

S12. Supplementary materials references

- Barnes, Richard. 2016. RichDEM: Terrain Analysis Software. <http://github.com/r-barnes/richdem>
- Berthier, E., Cabot, V., Vincent, C., and Six, D., 2016, Decadal Region-Wide and Glacier-Wide Mass Balances Derived from Multi-Temporal ASTER Satellite Digital Elevation Models . Validation over the Mont-Blanc Area: *frontiers in Earth Science*, v. 4, p. 1–16, doi:10.3389/feart.2016.00063.
- Bieniek, P.A., Bhatt, U.S., Walsh, J.E., Rupp, T.S., Zhang, J., Krieger, J.R., and Lader, R., 2016, Full access dynamical downscaling of ERA-interim temperature and precipitation for Alaska: *Journal of Applied Meteorology and Climatology*, v. 55, p. 635–654, doi:10.1175/JAMC-D-15-0153.1.
- Dussaillant, I., Berthier, E., Brun, F., Masiokas, M., Hugonnet, R., Favier, V., Rabatel, A., Pitte, P. and Ruiz, L., 2019, Two decades of glacier mass loss along the Andes, *Nature Geoscience*, 12(10), 802–808, doi:10.1038/s41561-019-0432-5.
- Ekström, G., and Stark, C.P., 2013, Simple scaling of catastrophic landslide dynamics.: *Science* (New York, N.Y.), v. 339, p. 1416–1419, doi:10.1126/science.1232887.
- Fairfield, J., and Leymarie, P., 1991, Drainage networks from grid digital elevation models: *Water Resources Research*, v. 27, p. 709–717, doi:10.1109/isie.1999.796880.

- Hock, R., 2003, Temperature index melt modelling in mountain areas: *Journal of Hydrology*, v. 282, p. 104–115, doi:10.1016/S0022-1694(03)00257-9.
- Iverson, R.M., George, D.L., and Logan, M., 2016, Debris flow runup on vertical barriers and adverse slopes: *Journal of Geophysical Research: Earth Surface*, v. 121, p. 2333–2357, doi:10.1002/2016JF003933.
- Jacquemart, M., and Loso, M., 2019, Catastrophic Glacier Collapse and Debris Flow at Flat Creek, Wrangell-St. Elias National Park and Preserve: *Alaska Park Science*, v. 18, p. 47–55.
- Kääb, A. et al., 2018, Massive collapse of two glaciers in western Tibet in 2016 after surge-like instability: *Nature Geoscience*, v. 11, p. 114–120, doi:10.1038/s41561-017-0039-7.
- Lippmann E. 2008. 4 Point light 10W, Technical Data Operating Instructions Version 4.19. Available from: <<http://www.l-gm.de>>. 23.01.2013.
- Loke, M.H., 2013. Rapid 2-D resistivity & IP inversion using the least-squares method: manual. Geotomo Softw., 28 October 2015 <http://www.geotomosoft.com>.
- Miles, E.S., Watson, C.S., Brun, F., Berthier, E., Esteves, M., Quincey, J., Miles, K.E., and Wagnon, P., 2018, Ablative and geomorphic effects of a supraglacial lake drainage and outburst event , Nepal Himalaya: *The Cryosphere Discuss.*, p. 1–25.
- Nuth, C., and Kääb, A., 2011, Co-registration and bias corrections of satellite elevation data sets for quantifying glacier thickness change: *Cryosphere*, v. 5, p. 271–290, doi:10.5194/tc-5-271-2011.
- Planet Team, 2018, Planet Application Program Interface: In Space for Life on Earth. San Francisco, CA. <https://api.planet.com>.
- Porter, C. et al., 2018, Arctic DEM:, doi:<https://doi.org/10.7910/DVN/OHHUKH>.
- Prochaska, A.B., Santi, P.M., Higgins, J.D., and Cannon, S.H., 2008, A study of methods to estimate debris flow velocity: *Landslides*, v. 5, p. 431–444, doi:10.1007/s10346-008-0137-0.

RGI Consortium, 2017, Randolph Glacier Inventory – A Dataset of Global Glacier Outlines: Version 6.0.:

Scheidl, C., McArdell, B.W., and Rickenmann, D., 2014, Debris-flow velocities and superelevation in a curved laboratory channel: Canadian Geotechnical Journal, v. 52, p. 305–317, doi:10.1139/cgj-2014-0081.

Shean, D.E., Alexandrov, O., Moratto, Z.M., Smith, B.E., Joughin, I.R., Porter, C., and Morin, P., 2016, An automated, open-source pipeline for mass production of digital elevation models (DEMs) from very-high-resolution commercial stereo satellite imagery: ISPRS Journal of Photogrammetry and Remote Sensing, v. 116, p. 101–117, doi:10.1016/j.isprsjprs.2016.03.012.